Atmos. Meas. Tech. Discuss., 8, 9209–9240, 2015
www.atmos-meas-tech-discuss.net/8/9209/2015/
doi:10.5194/amtd-8-9209-2015

Atmospheric Measurement Techniques Discussions
Open Access

Smithsonian Astrophysical Observatory Ozone Mapping and Profiler Suite (SAO OMPS) formaldehyde retrieval

G. González Abad[1], A. Vasilkov[2], C. Seftor[2], X. Liu[1], and K. Chance[1]

[1]Harvard-Smithsonian Center for Astrophysics, Cambridge, MA, USA
[2]NASA Goddard Space Flight Center, Greenbelt, MD, USA

Received: 11 August 2015 – Accepted: 17 August 2015 – Published: 7 September 2015

Correspondence to: G. González Abad (ggonzalezabad@cfa.harvard.edu)

Published by Copernicus Publications on behalf of the European Geosciences Union.

Abstract

This paper presents our new formaldehyde (H_2CO) retrievals, obtained from spectra recorded by the nadir instrument of the Ozone Mapping and Profiler Suite (OMPS) flown on-board NASA's Suomi National Polar-orbiting Partnership (SUOMI-NPP) satellite. Our algorithm is similar to the one currently in place for the production of NASA's Ozone Monitoring Instrument (OMI) operational H_2CO product. We are now able to produce a consistent set of long term data from two different instruments that share a similar concept. The ongoing overlap period between OMI and OMPS offers a perfect opportunity to study the consistency between both data sets. The different spatial and spectral resolution of the instruments is a source of discrepancy in the retrievals despite the similarity of the physic assumptions of the algorithm. We have concluded that the reduced spectral resolution of OMPS in comparison with OMI is not a significant obstacle in obtaining good quality retrievals. Indeed, the improved signal to noise ratio (SNR) of OMPS with respect to OMI helps to reduce the noise of the retrievals performed using OMPS spectra. However, the size of OMPS spatial pixels imposes a limitation in the capability to distinguish particular features of H_2CO that are discernible with OMI. With root mean square (RMS) residuals $\sim 5 \times 10^{-4}$ for individual pixels we estimate the detection limit to be about 7.5×10^{15} molecules cm^{-2}. Total vertical column densities (VCD) errors for individual pixels range between 40 % for pixels with high concentrations to 100 % or more for pixels with concentrations at or below the detection limit. We compare different OMI products with our OMPS product using one year of data, between September 2012 and September 2013. The seasonality of the retrieved slant columns is captured similarly by all products but there are discrepancies in the values of the VCDs. The mean biases among the two OMI products and our OMPS product are 21 % between OMI SAO and OMPS SAO and 38 % between OMI BIRA and OMPS SAO for eight selected regions.

AMTD
8, 9209–9240, 2015

1 Introduction

H_2CO is ubiquitous in the Earth's troposphere. Background levels in remote regions with concentrations below 1 ppb are due to methane (CH_4) oxidation. Over the continents, hotspots of enhanced concentrations are found due to oxidation of short-lived non-methane volatile organic compounds (NMVOCs) of anthropogenic, biogenic, and pyrogenic origin (secondary sources) or directly emitted by wild fires or industrial activities (primary sources). Concentrations of H_2CO over these hotspots can reach boundary layer levels of 5 ppb or higher (Houweling et al., 1998; Kanakidou et al., 2005; Lowe and Schmidt, 1983; Parrish et al., 2012).

The importance of H_2CO as an atmospheric trace gas resides in its influence in the chemical pathways of tropospheric ozone (O_3) and in the relationship with the concentration of hydroxyl radicals (OH), the main tropospheric oxidant (Anderson et al., 1996). Due to its high reactivity it has a short tropospheric lifetime of few hours (Brune et al., 1999) making it a useful proxy for NMVOCs emissions in satellite observations and for the estimation of top-down emission inventories of isoprene (Barkley et al., 2008; Fu et al., 2007; Marais et al., 2012; Stavrakou et al., 2009a, b; Zhu et al., 2014). High concentrations of H_2CO can be dangerous to human health, causing eye, nose and throat irritation. It is also known to be a human carcinogen. Fortunately, such high concentrations are not found in the open air (Liteplo et al., 2002) but are from cigarette smoking, pressed-wood products or fuel-burning appliances.

With UV nadir instruments we can sample concentrations in the trophosphere, where most of the atmospheric H_2CO is located. The first global H_2CO measurements using UV radiation were reported by Chance et al. (2000), using Global Ozone Monitoring Experiment (GOME) spectra. Since this seminal work, measurements of tropospheric H_2CO have been obtained using data recorded by the SCanning Imaging Absorption spectrometer for Atmospheric CHartography (SCIAMACHY), GOME-2 instruments and OMI (De Smedt et al., 2008, 2012; González Abad et al., 2015; Hewson et al., 2015; Kurosu et al., 2004; Palmer et al., 2001; Vrekoussis et al., 2010; Wittrock et al., 2006)

AMTD
8, 9209–9240, 2015

and now OMPS (this work and Li et al., 2015). Having overlapping retrievals from OMI and OMPS opens the possibility of building a long term data set of H_2CO using similar retrieval algorithms and having a period of cross calibration to allow us to extract valuable conclusions about the performance of both instruments that will be of great value for future low earth orbit (LEO) and geostationary missions such as the Trophospheric Emissions: Monitoring of Pollution (TEMPO, Chance et al., 2013).

Section 2 includes the description of the SAO OMPS H_2CO retrievals. We describe the characteristics of the instrument, the spectral fitting, the calculation of VCDs by using air mass factors (AMFs) and the reference sector normalization of the VCDs. Section 3 presents the error analysis for the VCDs. Section 4 describes the comparison between NASA's OMI operational retrieval and the OMPS product. The conclusions are in Sect. 5.

2 SAO OMPS H_2CO observations

2.1 The OMPS-NM instrument

The OMPS Nadir Mapper (OMPS-NM) is one of the three sensors that compose the OMPS suite of instruments. OMPS-NM was launched on-board the Suomi National Polar-orbiting Partnership (Suomi-NPP) satellite the 28 October 2011. Suomi-NPP orbits the Earth at an altitude of 824 km on a polar Sun-synchronous orbit with an inclination of 98.7° (Flynn et al., 2014). Its equator crossing time in the ascending node is 13:30 local time (LT) which places it close to the afternoon satellites of NASA's A-Train constellation, including Aura. Aura's hosts the UV visible spectrometer OMI (Levelt et al., 2006), thus offering a great opportunity for the comparison of the retrievals obtained from both instruments.

The OMPS-NM sensor combines a single grating and a 340 × 740 pixel charge-coupled device (CCD) array detector. It measures UV radiation covering the spectral range between 300 and 380 nm with a pixel sampling of 0.42 nm and a full width half

AMTD
8, 9209–9240, 2015

maximum (FWHM) of 1 nm. It has an instantaneous cross-track field of view (FOV) of approximately 110°, corresponding to 2800 km at the Earth's surface, providing global daily coverage. For this study we are using the OMPS-NM Earth science mode, where measurements are combined in 35 cross-track macropixels given a spatial size of the nadir pixel of 50 km (cross-track) by 50 km (along-track), with an integration period for each measurement of 7.6 s (Dittman et al., 2002; Seftor et al., 2014). The CCD readout is split in the center so that measurements of the central pixel are split, resulting in 36 cross-track pixel positions.

2.2 SAO OMPS H_2CO retrieval

To obtain H_2CO VCDs our algorithm follows a two step approach. First we perform a direct spectral fit of the measured radiance to obtain slant column densities (SCDs) using the basic optical absorption spectroscopy approach (BOAS, Chance, 1998). The second step converts SCDs to VCDs using look-up tables of precomputed scattering weights to calculate air mass factors (AMFs). The SAO OMPS H_2CO algorithm is similar to the SAO OMI H_2CO retrieval described in González Abad et al. (2015). Modifications are reduced to the minimum required to deal with particular aspects of the OMPS-NM instrument, to produce a long-term data set that is as consistent as possible. A more detailed description of the OMI algorithm is in Sect. 2 of González Abad et al. (2015). Here we will briefly describe the characteristics of the OMPS SAO H_2CO retrieval.

2.2.1 Spectral fitting

We have performed a series of studies to select the most suitable fitting window and fitting parameters for OMPS H_2CO. Our main interest was to reduce the correlation between H_2CO columns and the rest of the fitting parameters, especially BrO. We optimized the fitting window at 327.7 to 356.0 nm, slightly different to that used in several GOME, GOME-2, SCIAMACHY and OMI retrievals, 328.5 to 356.5 nm

AMTD
8, 9209–9240, 2015

(De Smedt et al., 2008, 2012; González Abad et al., 2015). Figure 1 shows the correlation among H_2CO and the rest of the fitted cross-sections. Even though the correlation between H_2CO and BrO shows two minimal bands between 325 and 326 and 330 and 331 nm two different considerations prevent the use of them. The first is from the increasing strength of O_3 cross-sections below 328 nm, apparent by increasing values of the correlation between H_2CO and O_3 in the middle and right top panels of Fig. 1. The second is from the increasing correlation with O_2-O_2. By choosing a fitting window starting at 327.7 nm we avoid the region with the strongest correlation with molecular Ring spectrum while having minimum correlation with O_3.

After selecting the fitting window we perform the direct fit of the measured radiance to the semi-empirical model of the top of atmosphere radiance described by Eq. (1). Prior to building the model we wavelength calibrate the radiance by cross correlating it with a high resolution solar spectrum (Chance and Kurucz, 2010).

$$\boldsymbol{I} = \left[(a\boldsymbol{I}_0 + \sum_i \alpha_i \boldsymbol{X}_i) e^{-\sum_j \alpha_j \boldsymbol{X}_j}\right] \sum_n \alpha_n X_n + \sum_m \alpha_m X_m \quad (1)$$

The radiance, $\boldsymbol{I}$, is calculated starting from a mean radiance reference, $\boldsymbol{I}_0$. We construct $\boldsymbol{I}_0$ using Earthshine radiances over the remote Pacific Ocean where H_2CO concentrations are assumed to be at background levels. These radiances are as close as possible to 165° W and were measured within one day of the orbit we are retrieving. With the set of selected radiances over the remote Pacific Ocean we calculate a mean radiance reference for each cross-track position. While computing the mean radiance reference I_0 we only consider spectra recorded between 30° S and 30° N. The reason behind using the mean radiance reference instead of the solar irradiance spectrum is to avoid cross-track stripes in the retrieval, a common problem in many sensors that use 2-D CCD array detectors (Veihelmann and Kleipool, 2006). The caveat of this solution is that effectively we are retrieving the differential SCDs (ΔSCDs) between the observation and the radiance reference spectra. To account for this fact we apply a cor-

AMTD
8, 9209–9240, 2015

rection based on a reference sector normalization which is described in higher detail in Sect. 2.4 (Khokhar et al., 2005).

In modeling the radiance we also include the effects of the Beer-Lambert law absorption ($e^{-\sum_j \alpha_j X_j}$) with contributions from H_2CO (Chance and Orphal, 2011), O_3 at two temperatures 228 and 295 K (Malicet et al., 1995), BrO (Wilmouth et al., 1999), NO_2 (Vandaele et al., 1998), the O_2–O_2 collision complex (Thalman and Volkamer, 2013) and molecular Ring (Chance and Spurr, 1997). We also include a correction term to account for instrument undersampling of the spectra ($\sum_i \alpha_i \boldsymbol{X}_i$) (Chance, 1998; Chance et al., 2005). The absorption cross-sections are convolved with the OMPS-NM slit functions. The functions were measured prior to launch using a tunable laser to scan the bandpasses of selected band centers at representative pixel locations on the focal plane; the resulting functions were then iterated to calculate a bandpass for each CCD pixel. The laser was tuned over a wavelength range of ±2 pixels for each of the OMPS-NM sensor band centers. Since the wavelength step size is coarse, approximately 0.4 pixels, 5 adjacent pixel responses were interpolated to a fine grid and combined to form a single observed band pass function. In Eq. (1) we are using two closure third order polynomials ($\sum_n \alpha_n X_n + \sum_m \alpha_m X_m$) to account for low frequency features of the spectra such as Rayleigh scattering and the effects of aerosols. In Eq. (1) α_x representents the fitting parameter while X_x represents the undersampling correction, the cross sections or the different orders of the polynomials. The characteristics of the spectral fitting are summarized in Table 1. To retrieve the SCDs we use a nonlinear least-squares inversion method implemented in the ELSUNC software (Lindström and Wedin, 1988) to minimize the cost function χ^2 defined as the weighted square difference between the measured and modeled radiance.

Figure 2 shows the result of the fitting for three pixels in orbit 3538 over the Americas. These three pixels have been chosen to illustrate how just with a visual inspection, when the amount of H_2CO is big enough, we can clearly distinguish the H_2CO signal in the fitting (two top panels with retrieved H_2CO concentrations of 1.8×10^{16} and 0.8×10^{16} respectively) while in the last case, as we approach the detection limit,

AMTD
8, 9209–9240, 2015

it is difficult to tell visually if there is measurable H_2CO and we must rely on statistics to obtain the information. Typical retrieved ΔSCDs range between -0.5×10^{15} and 2×10^{16} molecules cm^{-2} for background levels and hotspots with fitting uncertainties about 4.0×10^{15}.

Figure 3 shows the ΔSCDs, the fitting uncertainty, the solar zenith angle (SZA) and the relative fitting uncertainty for this orbit. The effect of the South Atlantic Anomaly (SAA) in the quality of the retrieval is evident in the ΔSCDs and the fitting uncertainties (swath lines 20–120). Note the increase in the fitting uncertainty as the SZAs increase. Excluding the SAA, the fitting uncertainty remains around 5×10^{15} molecules cm^{-2} or less for SZAs below 70°. With typical RMS values of $\sim 5 \times 10^{-4}$ we estimate the detection limit of the retrieval $\sim 7.5 \times 10^{15}$ molecules cm^{-2}. As the background concentration due to CH_4 oxidation in remote regions is 2 to 7×10^{15} molecules cm^{-2}, the retrieval is unable to clearly resolve background concentrations. This situation is evident if we consider the standard deviation over the remote Pacific Ocean which is around 4×10^{15} molecules cm^{-2}, similar to the concentrations expected in remote regions.

2.2.2 Slant column to vertical column calculation

The proportionality between VCDs and SCDs can be expressed via AMFs (Eq. 2). The AMFs contain information, some of it a priori, about the state of the atmosphere (gas concentrations, clouds and aerosols), the surface of the spatial pixel and the geometry of the retrieval.

$$\mathrm{VCD} = \frac{\mathrm{SCD}}{\mathrm{AMF}} \tag{2}$$

To compute AMFs we follow the theoretical approach described by Palmer et al. (2001). The main idea is that for weak trace gas absorption such as that of H_2CO, we can describe the AMFs as the combination of a shape factor containing information about the vertical distribution of H_2CO concentrations and the scattering weights ($w(z)$) describing how the radiation is transmitted throughout different layers of the at-

AMTD
8, 9209–9240, 2015

mosphere. $w(z)$ are functions of the geometry of the observation (SZA, viewing zenith angle (VZA) and relative azimuth angle (RAA)), the altitude, the O_3 profile, since it has the most significant absorption features, the aerosol load, the surface properties (reflectance and altitude) and the characteristics of the clouds present in the scene if any (cloud fraction and cloud pressure). In our algorithm cloudy pixels are treated by considering the independent pixel approximation (Martin et al., 2002). In this approximation the pixel $w(z)$ is the combination of the cloud free scattering weight (w_{clear}) and the cloudy scattering weight (w_{cloud}) as shown in Eq. (3) for a given altitude. w_{clear} is function of the geometry of the problem, surface albedo (a_s) and surface elevation (h_s) and the altitude while w_{cloud} depends on the cloud albedo (a_c), defined here as 0.8, and the cloud centroid pressure (c_p) and the altitude. Φ is the radiative cloud fraction.

$$w(z) = (1 - \Phi) \cdot w_{\text{clear}}(z, a_s, h_s) + \Phi \cdot w_{\text{cloud}}(z, a_c, c_p), \quad (3)$$

We extract the a priori H_2CO information from the same monthly GEOS-Chem (Bey et al., 2001) climatology we are using in our SAO OMI H_2CO retrieval. $w(z)$ are precomputed using VLIDORT (Spurr, 2006) and saved in look-up tables. These tables consider the $w(z)$ dependency with viewing geometry (SZA,VZA and RAA), surface altitude, surface reflectance and cloud properties. Information about the pixel surface reflectance is obtained from the Total Ozone Mapping Instrument (TOMS) climatology (C. Ahn, personal communication, 2015) while for cloud information (Φ and c_p) we use the cloud product developed by Vasilkov et al. (2014). Given the small variation of $w(z)$ within the fitting window (less than 7 %) we are considering $w(z)$ at one wavelength (λ), 340 nm, which we consider representative of their mean value within the fitting window. A detailed description of AMF calculations can be found in González Abad et al. (2015).

2.2.3 Reference sector normalization of VCDs

We are retrieving ΔSCDs due to the fact that we are using a radiance reference as starting point in the modeling of radiances. To obtain SCDs starting from these ΔSCDs

AMTD
8, 9209–9240, 2015

we calculate a normalization to modeled values. We work out the difference between the retrieval over the Pacific Ocean and the GEOS-Chem climatology. The process, inspired by earlier work by Khokhar et al. (2005) and De Smedt et al. (2008), is described in detail in González Abad et al. (2015). Here we mention the essential steps and ideas behind it.

Using the same radiance reference we perform two retrievals. One retrieval is for the orbit of interest, let us say a satellite flight over Africa and Europe, and the second one is the retrieval of the orbit we used to compute the radiance reference which is always over the remote Pacific Ocean. Using the second retrieval and the monthly GEOS-Chem climatology we work out a latitudinal dependent correction which accounts for the difference between the ΔSCDs and the model SCDs. We then assume that this correction is longitudinally constant so that we can apply the correction to results from the orbit of interest retrieval. Before applying the correction we take into account the particularities of each scene by using the information contained in the AMFs. Equations (4) and (5) summarize the basic operations involved in the process.

$$\mathrm{Corr(lat)} = \mathrm{MEDIAN}\left[(\mathrm{VCD_{GEOS}} \times \mathrm{AMF}_j) - \Delta\mathrm{SCD}_j\right] \quad (4)$$

We work out the amplitude of the correction at 500 latitude grid points extending from 90° N to 90° S. To obtain the value for each grid point we consider the median value of all j pixels of the radiance reference orbit whose central latitudes are in between any given couple of contiguous grid points. After interpolating the correction to the latitude value of each pixel (i) in the orbit of interest we apply the information contained in the particular AMF to that pixel to obtain the reference sector corrected VCD.

$$\mathrm{VCD}_i = \frac{\mathrm{Corr(lat}_i) + \Delta\mathrm{SCD}_i}{\mathrm{AMF}_i} \quad (5)$$

Figure 4 shows ΔVCDs, VCDs, ΔVCDs fitting uncertainty and RMS for orbit 6202 a January 2013 overpass of Africa and Europe. Enhanced concentrations in the middle of the orbit correspond to hot spots over Central Africa.

AMTD
8, 9209–9240, 2015

3 Error analysis

For an individual pixel VCD the associated error ($\varepsilon_{\mathrm{VCD}}$) is given by Eq. (6), which assumes no correlation between terms. Given the small contributions arising from correlations this is a good approximation for the description of the VCD error (Boersma et al., 2004).

$$\varepsilon^2_{\mathrm{VCD}} = \frac{\varepsilon^2_{\Delta\mathrm{SCD}_{\mathrm{random}}}}{\mathrm{AMF}^2} + \frac{\varepsilon^2_{\Delta\mathrm{SCD}_{\mathrm{sys}}}}{\mathrm{AMF}^2} + \left(\frac{\mathrm{Corr}}{\mathrm{AMF}^2}\right)^2 \varepsilon^2_{\mathrm{AMF}} + \frac{\varepsilon^2_{\mathrm{Corr}}}{\mathrm{AMF}^2} \tag{6}$$

In Eq. (6) $\varepsilon_{\Delta\mathrm{SCD}_{\mathrm{ramdon}}}$ is the random component of the spectral fitting process. It can be estimated by considering the residuals of the fitting process according to Eq. (7) which takes into consideration the diagonal term of the covariance matrix for H_2CO ($\mathbf{C}_j$) and the RMS fitting residual weighted by the degrees of freedom. This method to estimate $\varepsilon_{\Delta\mathrm{SCD}_{\mathrm{ramdon}}}$ also includes contributions from systematic errors that consistently show up in the fitting residuals. To evaluate them we have computed an average residual ("common mode") for each cross track position and included it in the semi-empirical calculation of the radiances (Eq. 1) as an extra term. The difference in the fitting uncertainty between retrievals performed with and without the common mode is about 25 %. We attribute this difference to systematic errors due to instrumental effects such as characterization of the instrumental line shape, wavelength calibration and stray light. As mentioned in Sect. 2.2.1, $\varepsilon_{\Delta\mathrm{SCD}_{\mathrm{ramdon}}}$ values range between 10 % over H_2CO hot spots to 100 % or more for pixels with low concentrations.

$$\varepsilon_{\mathrm{random}} = \mathrm{RMS}^2 \left(\frac{m}{m-n}\right)(\mathbf{C}_j \mathbf{C}_j) \tag{7}$$

We have evaluated the systematic component of ΔSCD error ($\varepsilon_{\Delta\mathrm{SCD}_{\mathrm{sys}}}$) considering only the error associated with the uncertainties of the different cross sections included in the semi-empirical model of the radiances (Eq. 1). Table 2 summarizes the uncertainties associated to each molecule as reported in the literature. Considering that the

AMTD
8, 9209–9240, 2015

uncertainties for different cross sections are not correlated we have found $\varepsilon_{\Delta SCD_{sys}}$ to be about 7 %.

To estimate the error associated with AMF calculations we have performed a sensitivity analysis that takes into account the uncertainties associated with cloud parameters, surface reflectance, terrain height and GEOS-Chem climatological profiles as well as the wavelength dependency of $w(s)$ within the fitting window. We already mentioned that the dependency with λ of $w(z)$ is weak, around 7 %, and by choosing a λ near the center of the fitting window, 340 nm, we estimate that the error due to the variation of $w(z)$ in the fitting window is about 4 %. In the UV spectral range, most surfaces reflect between 1 and 10 % of the incoming light. The errors of the TOMS surface climatology are estimated to be around 40 % which translates to an error of 6 % in the AMF for a typical surface with an albedo of 0.03. Brighter surfaces such as deserts with albedos of 0.1 will have an AMF error of 14 % while for a snowy pixel with an albedo of 0.4 the AMF error will be about 26 %. A change in the cloud pressure from 800 to 900 hPa will imply a change in the AMF from 0.6 to 1.2. The cloud product we are using is derived from analysis of the rotational Raman scattering around 350 nm (Vasilkov et al., 2014). Errors of the cloud centroid pressure are estimated to be about 50 hPa which translates to variations in the AMF values of 23 %. A change in the cloud fraction of 0.1 for a cloud pressure of 800 hPa will change the AMF by 25 %. To finish the sensitivity analysis of the AMF calculation we tested the impact of the a priori profiles of H_2CO. Assuming a bias in the GEOS-Chem profiles of 10 % (Millet et al., 2006; Barkley et al., 2011) we have found that the AMFs may change in different regions up to 16 %. Considering the contributions from all these factors we estimate ε_{AMF} to be about 38 % where the cloud parameters are the most significant source of uncertainty.

Finally we consider ε_{Corr}, the error associated with the GEOS-Chem climatology used to perform the reference sector correction. As mentioned above this climatology is estimated to have a 10 % error which we have assumed to be directly carried over to the final H_2CO VCDs. This assumption intentionally provides a high error estimate.

AMTD
8, 9209–9240, 2015

To summarize, users of this product should assume that a typical pixel VCD will have an uncertainty ranging between 40 and 100 % for hot spots and background level concentration pixels respectively.

4 Comparison between OMI and OMPS H_2CO retrievals

We have compared our retrieval with two OMI retrievals using monthly mean averages VCDs at a spatial resolution of $0.25^\circ \times 0.25^\circ$ for the time period August 2012 to August 2013. We have only considered pixels with SZA smaller than 70° and radiative cloud fraction below 40 %. OMI pixels affected by the row anomaly were discarded. The OMI retrievals used for this comparison exercise are the Belgian Institute for Space Aeronomy (BIRA) retrieval (De Smedt et al., 2012) version v14 downloaded from the TEMIS webpage (http://h2co.aeronomie.be/) and the SAO OMI retrieval v3.0.2 (González Abad et al., 2015) available from NASA's web page (http://disc.sci.gsfc.nasa.gov/Aura/data-holdings/OMI/omhcho_v003.shtml).

Two of the most significant advantages of comparing OMPS with OMI are the close overpass time for both instruments, around 01:30 p.m. LT, and the similar concepts of the instruments. Both designs use 2-D CCD detectors. A significant disadvantage is their difference in the spatial pixel size. OMI has a nadir pixel size of 24×13 km while OMPS, in the configuration we are using, has a nadir pixel size of 50×50 km. Figure 5 shows the eight regions we have selected for comparison. The limits are explicitly shown in Table 3.

The three retrievals are able to capture the seasonality of H_2CO columns, showing similar patterns, as seen in Fig. 6 where we have plotted the time series of monthly means for the different regions. The error bars are the standard deviations of the pixels included in the calculation of monthly means. The three retrievals, however, observe different amplitudes of seasonal variation. There is also a bias that can be significant for particular months and regions. The big difference between the BIRA and SAO retrievals over the Pacific Ocean is induced by the underlying difference of the models used

AMTD
8, 9209–9240, 2015

for the reference sector correction. As expected, the differences in the results of the retrieval are bigger between the OMI BIRA and the OMPS SAO than between OMI SAO and OMPS SAO. The absolute mean offset between the OMPS SAO retrieval and the OMI BIRA is 38 % while between OMI and OMPS SAO retrievals it is approximately 21 %.

While these mean absolute offsets give us an idea of how close the retrievals are from a general perspective it is more interesting to consider the differences for particular regions. For example, in the results for Southern Africa in Fig. 6 both SAO retrievals consistently produce smaller values than the BIRA retrieval between March and October, around 60 % lower, while for Southeastern Asia the situation is reversed with the SAO retrievals having higher values than the BIRA retrieval. Figure 7 summarizes this situation for all regions. We have plotted the offset for each region and month between OMPS and OMI retrievals. It is clear that to obtain a better idea of the accuracy of the different retrievals independent validation exercises are necessary, but they are out of the scope of this paper.

The error bars of Fig. 6 contain information about the variation within each region and month expressed as the standard deviation of the VCDs considered for each monthly mean calculation. In general we observe a stronger variability within one region and one month in the BIRA retrieval than in the SAO retrievals. The average VCDs variability for the retrievals considering all regions and months is 2.6×10^{15} molecules cm^{-2} for OMI BIRA, 1.9×10^{15} molecules cm^{-2} for OMI SAO and 2.2×10^{15} molecules cm^{-2} for the OMPS SAO retrieval. We have included Fig. 8 showing the standard deviation for each retrieval, month and region.

5 Conclusions

We have developed a new OMPS H_2CO retrieval by adapting the OMI SAO H_2CO retrieval to OMPS-NM. Our two-step retrieval includes the direct fitting of radiances to obtain ΔSCDs, the calculation of AMFs to convert ΔSCDs to ΔVCDs and the application

AMTD
8, 9209–9240, 2015

of a reference sector correction based on a monthly climatology derived from GEOS-Chem simulations to obtain the final VCDs. Despite the reduced spectral resolution of OMPS (1 nm) with respect other sensors like OMI or GOME-2 the retrievals presented here provide compelling evidence of the suitability of OMPS-NM sensor to perform H_2CO retrievals. Even more, given the good SNR of OMPS-NM the retrieval has reduced noise compared with OMI retrievals and an improved detection limit, 7.5×10^{15} vs. 1×10^{16} molecules cm^{-2} in the case of the OMI SAO retrieval. The improved SNR comes in part from the bigger number of photons captured by larger spatial pixels by OMPS-NM with respect to OMI pixels. Typical values of the OMPS H_2CO VCDs range between 0.5×10^{16} and 2×10^{16} molecules cm^{-2} with associated errors of around 40 % over pixels with high concentrations that increase to 100 % or even more for pixels with low concentrations.

We have compared the OMPS SAO retrieval with OMI retrievals developed at BIRA and SAO. While all three retrievals similarly capture the general trends of seasonal variation they show significant differences in the amplitude of the seasonal signals with significant offsets between them as well. As expected, the agreement between the SAO retrievals is better than the agreement between the SAO OMPS and BIRA OMI retrieval. The mean offset for selected regions with strong seasonal variations plus the remote Pacific Ocean is 21 % between the SAO retrievals and 38 % between the SAO OMPS and OMI BIRA retrievals. Obviously, to have an assessment of the absolute accuracy of the retrieval it is necessary to perform validation studies with independent in situ data. These studies are out of the scope of this paper but will constitute part of ongoing efforts to validate the latest version of the SAO OMI retrieval.

Finally we want to highlight the benefit of having similar retrievals from two instruments overlaping in time. The data record for OMI already extends for more than 10 years. OMPS was launched on board the SUOMI-NPP satellite in October 2011 and it is therefore in the early stages of its operational life. The ongoing overlapping period between both instruments offers a great opportunity to construct a consistent extended long term data set. To fully exploit the scientific benefits from this opportu-

AMTD
8, 9209–9240, 2015

nity further studies analyzing the impact of different spectral and spatial resolutions in the retrievals of H_2CO are necessary. The prospect of other OMPS instruments to be launched in future missions of the National Oceanic and Atmospheric Administration (NOAA) such as the Joint Polar Satellite System (JPSS) will create the possibility of creating a multi decadal set of consistent measurements of H_2CO from afternoon low earth orbit platforms.

Acknowledgements. This study is supported by NASA Atmospheric Composition Program/Aura Science Team (NNX11AE58G) and internal Smithsonian Institution funds from the Consortium for Unlocking the Mysteries of the Universe. The Dutch-Finnish OMI instrument is part of the NASA EOS Aura satellite payload. The OMI Project is managed by NIVR and KNMI in the Netherlands. We acknowledge the OMI and OMPS projects for providing data used in this study. We thank Kai Yang for his valuable input understanding the characteristics of OMPS-NM.

References

Anderson, L. G., Lanning, J. A., Barrell, R., Miyagishima, J., Jones, R. H., and Wolfe, P.: Sources and sinks of formaldehyde and acetaldehyde: An analysis of Denver's ambient concentration data, Atmos. Environ., 30, 2113–2123, doi:10.1016/1352-2310(95)00175-1, 1996. 9211

Barkley, M. P., Palmer, P. I., Kuhn, U., Kesselmeier, J., Chance, K., Kurosu, T. P., Martin, R. V., Helmig, D., and Guenther, A.: Net ecosystem fluxes of isoprene over tropical South America inferred from Global Ozone Monitoring Experiment (GOME) observations of HCHO columns, J. Geophys. Res.-Atmos., 113, D20304, doi:10.1029/2008JD009863, 2008. 9211

Barkley, M. P., Palmer, P. I., Ganzeveld, L., Arneth, A., Hagberg, D., Karl, T., Guenther, A., Paulot, F., Wennberg, P. O., Mao, J., Kurosu, T. P., Chance, K., Müller, J.-F., De Smedt, I., Van Roozendael, M., Chen, D., Wang, Y., and Yantosca, R. M.: Can a "state of the art" chemistry transport model simulate Amazonian tropospheric chemistry?, J. Geophys. Res.-Atmos., 116, D16302, doi:10.1029/2011JD015893, 2011. 9220

Bey, I., Jacob, D. J., Yantosca, R. M., Logan, J. A., Field, B. D., Fiore, A. M., Li, Q., Liu, H. Y., Mickley, L. J., and Schultz, M. G.: Global modeling of tropospheric chemistry with assimilated meteorology: Model description and evaluation, J. Geophys. Res.-Atmos., 106, 23073–23095, doi:10.1029/2001JD000807, 2001. 9217

AMTD
8, 9209–9240, 2015

Boersma, K. F., Eskes, H. J., and Brinksma, E. J.: Error analysis for tropospheric NO_2 retrieval from space, J. Geophys. Res.-Atmos., 109, D04311, doi:10.1029/2003JD003962, 2004. 9219

Brune, W. H., Tan, D., Faloona, I. F., Jaeglé, L., Jacob, D. J., Heikes, B. G., Snow, J., Kondo, Y., Shetter, R., Sachse, G. W., Anderson, B., Gregory, G. L., Vay, S., Singh, H. B., Davis, D. D., Crawford, J. H., and Blake, D. R.: OH and HO_2 chemistry in the North Atlantic free troposphere, Geophys. Res. Lett., 26, 3077–3080, doi:10.1029/1999GL900549, 1999. 9211

Chance, K.: Analysis of BrO measurements from the Global Ozone Monitoring Experiment, Geophys. Res. Lett., 25, 3335–3338, doi:10.1029/98GL52359, 1998. 9213, 9215

Chance, K. and Kurucz, R. L.: An improved high-resolution solar reference spectrum for earth's atmosphere measurements in the ultraviolet, visible, and near infrared, J. Quant. Spectrosc. Ra., 111, 1289–1295, doi:10.1016/j.jqsrt.2010.01.036, 2010. 9214, 9230

Chance, K. and Orphal, J.: Revised ultraviolet absorption cross sections of H_2CO for the HITRAN database, J. Quant. Spectrosc. Ra., 112, 1509–1510, doi:10.1016/j.jqsrt.2011.02.002, 2011. 9215, 9230, 9231

Chance, K., Palmer, P. I., Spurr, R. J. D., Martin, R. V., Kurosu, T. P., and Jacob, D. J.: Satellite observations of formaldehyde over North America from GOME, Geophys. Res. Lett., 27, 3461–3464, doi:10.1029/2000GL011857, 2000. 9211

Chance, K., Kurosu, T. P., and Sioris, C. E.: Undersampling correction for array detector-based satellite spectrometers, Appl. Opt., 44, 1296–1304, doi:10.1364/AO.44.001296, 2005. 9215, 9230

Chance, K., Liu, X., Suleiman, R. M., Flittner, D. E., Al-Saadi, J., and Janz, S. J.: Tropospheric emissions: monitoring of pollution (TEMPO), 88660D, doi:10.1117/12.2024479, 2013. 9212

Chance, K. V. and Spurr, R. J. D.: Ring effect studies: Rayleigh scattering, including molecular parameters for rotational Raman scattering, and the Fraunhofer spectrum, Appl. Opt., 36, 5224–5230, doi:10.1364/AO.36.005224, 1997. 9215, 9230, 9231

De Smedt, I., Müller, J.-F., Stavrakou, T., van der A, R., Eskes, H., and Van Roozendael, M.: Twelve years of global observations of formaldehyde in the troposphere using GOME and SCIAMACHY sensors, Atmos. Chem. Phys., 8, 4947–4963, doi:10.5194/acp-8-4947-2008, 2008. 9211, 9214, 9218

De Smedt, I., Van Roozendael, M., Stavrakou, T., Müller, J.-F., Lerot, C., Theys, N., Valks, P., Hao, N., and van der A, R.: Improved retrieval of global tropospheric formaldehyde columns

AMTD
8, 9209–9240, 2015

from GOME-2/MetOp-A addressing noise reduction and instrumental degradation issues, Atmos. Meas. Tech., 5, 2933–2949, doi:10.5194/amt-5-2933-2012, 2012. 9211, 9214, 9221
Dittman, M. G., Ramberg, E., Chrisp, M., Rodriguez, J. V., Sparks, A. L., Zaun, N. H., Hendershot, P., Dixon, T., Philbrick, R. H., and Wasinger, D.: Nadir ultraviolet imaging spectrometer for the NPOESS Ozone Mapping and Profiler Suite(OMPS), in: Proceedings of SPIE, 4814, 111–119, 2002. 9213
Flynn, L., Long, C., Wu, X., Evans, R., Beck, C. T., Petropavlovskikh, I., McConville, G., Yu, W., Zhang, Z., Niu, J., Beach, E., Hao, Y., Pan, C., Sen, B., Novicki, M., Zhou, S., and Seftor, C.: Performance of the Ozone Mapping and Profiler Suite (OMPS) products, J. Geophys. Res.-Atmos., 119, 6181–6195, doi:10.1002/2013JD020467, 2014. 9212
Fu, T.-M., Jacob, D. J., Palmer, P. I., Chance, K., Wang, Y. X., Barletta, B., Blake, D. R., Stanton, J. C., and Pilling, M. J.: Space-based formaldehyde measurements as constraints on volatile organic compound emissions in east and south Asia and implications for ozone, J. Geophys. Res.-Atmos., 112, D06312, doi:10.1029/2006JD007853, 2007. 9211
González Abad, G., Liu, X., Chance, K., Wang, H., Kurosu, T. P., and Suleiman, R.: Updated Smithsonian Astrophysical Observatory Ozone Monitoring Instrument (SAO OMI) formaldehyde retrieval, Atmos. Meas. Tech., 8, 19–32, doi:10.5194/amt-8-19-2015, 2015. 9211, 9213, 9214, 9217, 9218, 9221
Hewson, W., Barkley, M. P., Gonzalez Abad, G., Bösch, H., Kurosu, T., and Spurr, R.: Development and characterisation of a state-of-the-art GOME-2 formaldehyde air-mass factor algorithm, Atmos. Meas. Tech. Discuss., 8, 1109–1150, doi:10.5194/amtd-8-1109-2015, 2015. 9211
Houweling, S., Dentener, F., and Lelieveld, J.: The impact of nonmethane hydrocarbon compounds on tropospheric photochemistry, J. Geophys. Res.-Atmos., 103, 10673–10696, doi:10.1029/97JD03582, 1998. 9211
Kanakidou, M., Seinfeld, J. H., Pandis, S. N., Barnes, I., Dentener, F. J., Facchini, M. C., Van Dingenen, R., Ervens, B., Nenes, A., Nielsen, C. J., Swietlicki, E., Putaud, J. P., Balkanski, Y., Fuzzi, S., Horth, J., Moortgat, G. K., Winterhalter, R., Myhre, C. E. L., Tsigaridis, K., Vignati, E., Stephanou, E. G., and Wilson, J.: Organic aerosol and global climate modelling: a review, Atmos. Chem. Phys., 5, 1053–1123, doi:10.5194/acp-5-1053-2005, 2005. 9211
Khokhar, M., Frankenberg, C., Roozendael, M. V., Beirle, S., Kuhl, S., Richter, A., Platt, U., and Wagner, T.: Satellite observations of atmospheric SO_2 from volcanic eruptions during the

AMTD
8, 9209–9240, 2015

time-period of 1996–2002, Adv. Space Res., 36, 879–887, doi:10.1016/j.asr.2005.04.114, 2005. 9215, 9218

Kurosu, T. P., Chance, K., and Sioris, C. E.: Preliminary results for HCHO and BrO from the EOS-Aura Ozone Monitoring Instrument, Proc. SPIE, 5652, 116–123, doi:10.1117/12.578606, 2004. 9211

Levelt, P. F., van den Oord, G. H. J., Dobber, M. R., Mälkki, A., Visser, H., de Vries, J., Stammes, P., Lundell, J. O. V., and Saari, H.: The ozone monitoring instrument, IEEE T. Geosci. Remote., 44, 1093–1101, doi:10.1109/TGRS.2006.872333, 2006. 9212

Li, C., Joiner, J., Krotkov, N. A., and Dunlap, L.: A new method for global retrievals of HCHO total columns from the Suomi National Polar-orbiting Partnership Ozone Mapping and Profiler Suite, Geophys. Res. Lett., 42, 2515–2522, doi:10.1002/2015GL063204, 2015. 9212

Lindström, P. and Wedin, P.-A.: Methods and software for nonlinear least squares problems, Technical report UMINF-133.87, Inst. of Information Processing, University of Umeå, Umeå, Sweden, 1–27, 1988. 9215

Liteplo, R. G., Beauchamp, R., Meek, M. E., and Chénier, R.: Concise International Chemical Assessment Document 40, Formaldehyde, Tech. rep., World Health Organization, available at: http://www.who.int/ipcs/publications/cicad/en/cicad40.pdf?ua=1 (last access: August 2015), 2002. 9211

Lowe, D. C. and Schmidt, U.: Formaldehyde (HCHO) measurements in the nonurban atmosphere, J. Geosphys. Res.-Oceans, 88, 10844–10858, doi:10.1029/JC088iC15p10844, 1983. 9211

Malicet, J., Daumont, D., Charbonnier, J., Parisse, C., Chakir, A., and Brion, J.: Ozone UV spectroscopy. II. Absorption cross-sections and temperature dependence, J. Atmos. Chem., 21, 263–273, doi:10.1007/BF00696758, 1995. 9215, 9230, 9231

Marais, E. A., Jacob, D. J., Kurosu, T. P., Chance, K., Murphy, J. G., Reeves, C., Mills, G., Casadio, S., Millet, D. B., Barkley, M. P., Paulot, F., and Mao, J.: Isoprene emissions in Africa inferred from OMI observations of formaldehyde columns, Atmos. Chem. Phys., 12, 6219–6235, doi:10.5194/acp-12-6219-2012, 2012. 9211

Martin, R. V., Chance, K., Jacob, D. J., Kurosu, T. P., Spurr, R. J. D., Bucsela, E., Gleason, J. F., Palmer, P. I., Bey, I., Fiore, A. M., Li, Q., Yantosca, R. M., and Koelemeijer, R. B. A.: An improved retrieval of tropospheric nitrogen dioxide from GOME, J. Geophys. Res.-Atmos., 107, ACH 9-1–ACH 9-21, doi:10.1029/2001JD001027, 2002. 9217

AMTD
8, 9209–9240, 2015

Millet, D. B., Jacob, D. J., Turquety, S., Hudman, R. C., Wu, S., Fried, A., Walega, J., Heikes, B. G., Blake, D. R., Singh, H. B., Anderson, B. E., and Clarke, A. D.: Formaldehyde distribution over North America: Implications for satellite retrievals of formaldehyde columns and isoprene emission, J. of Geophys. Res.-Atmos., 111, D24S02, doi:10.1029/2005JD006853, 2006. 9220

Palmer, P. I., Jacob, D. J., Chance, K., Martin, R. V., Spurr, R. J. D., Kurosu, T. P., Bey, I., Yantosca, R., Fiore, A., and Li, Q.: Air mass factor formulation for spectroscopic measurements from satellites: Application to formaldehyde retrievals from the Global Ozone Monitoring Experiment, J. Geophys. Res.-Atmos., 106, 14539–14550, doi:10.1029/2000JD900772, 2001. 9211, 9216

Parrish, D. D., Ryerson, T. B., Mellqvist, J., Johansson, J., Fried, A., Richter, D., Walega, J. G., Washenfelder, R. A., de Gouw, J. A., Peischl, J., Aikin, K. C., McKeen, S. A., Frost, G. J., Fehsenfeld, F. C., and Herndon, S. C.: Primary and secondary sources of formaldehyde in urban atmospheres: Houston Texas region, Atmos. Chem. Phys., 12, 3273–3288, doi:10.5194/acp-12-3273-2012, 2012. 9211

Seftor, C. J., Jaross, G., Kowitt, M., Haken, M., Li, J., and Flynn, L. E.: Postlaunch performance of the Suomi National Polar-orbiting Partnership Ozone Mapping and Profiler Suite (OMPS) nadir sensors, J. Geophys. Res.-Atmos., 119, 4413–4428, doi:10.1002/2013JD020472, 2014. 9213, 9235, 9236

Spurr, R. J.: VLIDORT: A linearized pseudo-spherical vector discrete ordinate radiative transfer code for forward model and retrieval studies in multilayer multiple scattering media, J. Quant. Spectrosc. RA., 102, 316–342, doi:10.1016/j.jqsrt.2006.05.005, 2006. 9217

Stavrakou, T., Müller, J.-F., De Smedt, I., Van Roozendael, M., van der Werf, G. R., Giglio, L., and Guenther, A.: Evaluating the performance of pyrogenic and biogenic emission inventories against one decade of space-based formaldehyde columns, Atmos. Chem. Phys., 9, 1037–1060, doi:10.5194/acp-9-1037-2009, 2009a. 9211

Stavrakou, T., Müller, J.-F., De Smedt, I., Van Roozendael, M., van der Werf, G. R., Giglio, L., and Guenther, A.: Global emissions of non-methane hydrocarbons deduced from SCIAMACHY formaldehyde columns through 2003–2006, Atmos. Chem. Phys., 9, 3663–3679, doi:10.5194/acp-9-3663-2009, 2009b. 9211

Thalman, R. and Volkamer, R.: Temperature dependent absorption cross-sections of O2-O2 collision pairs between 340 and 630 nm and at atmospherically relevant pressure, Phys. Chem. Chem. Phys., 15, 15371–15381, doi:10.1039/C3CP50968K, 2013. 9215, 9230, 9231

AMTD
8, 9209–9240, 2015

Vandaele, A., Hermans, C., Simon, P., Carleer, M., Colin, R., Fally, S., Mérienne, M., Jenouvrier, A., and Coquart, B.: Measurements of the NO_2 absorption cross-section from 42 000 cm^{-1} to 10 000 cm^{-1} (238–1000 nm) at 220 K and 294 K, J. Quant. Spectrosc. Ra., 59, 171–184, doi:10.1016/S0022-4073(97)00168-4, 1998. 9215, 9230, 9231

Vasilkov, A., Joiner, J., and Seftor, C.: First results from a rotational Raman scattering cloud algorithm applied to the Suomi National Polar-orbiting Partnership (NPP) Ozone Mapping and Profiler Suite (OMPS) Nadir Mapper, Atmos. Meas. Tech., 7, 2897–2906, doi:10.5194/amt-7-2897-2014, 2014. 9217, 9220

Veihelmann, B. and Kleipool, Q.: Reducing Along-Track Stripes in OMI-Level 2 Products, Technical report TN-OMIE-KNMI-785, KNMI, available at: http://disc.sci.gsfc.nasa.gov/Aura/data-holdings/OMI/documents/v003/RD08_TN785_i1_Reducing_AlongTrack_Stripes.pdf, 2006. 9214

Vrekoussis, M., Wittrock, F., Richter, A., and Burrows, J. P.: GOME-2 observations of oxygenated VOCs: what can we learn from the ratio glyoxal to formaldehyde on a global scale?, Atmos. Chem. Phys., 10, 10145–10160, doi:10.5194/acp-10-10145-2010, 2010. 9211

Wilmouth, D. M., Hanisco, T. F., Donahue, N. M., and Anderson, J. G.: Fourier Transform Ultraviolet Spectroscopy of the A 2Π3/2 ← X 2Π3/2 Transition of BrO†, J. Phys. Chem. A, 103, 8935–8945, doi:10.1021/jp991651o, 1999. 9215, 9230, 9231

Wittrock, F., Richter, A., Oetjen, H., Burrows, J. P., Kanakidou, M., Myriokefalitakis, S., Volkamer, R., Beirle, S., Platt, U., and Wagner, T.: Simultaneous global observations of glyoxal and formaldehyde from space, Geophys. Res. Lett., 33, L16804, doi:10.1029/2006GL026310, 2006. 9211

Zhu, L., Jacob, D. J., Mickley, L. J., Marais, E. A., Cohan, D. S., Yoshida, Y., Duncan, B. N., González Abad, G., and Chance, K. V.: Anthropogenic emissions of highly reactive volatile organic compounds in eastern Texas inferred from oversampling of satellite (OMI) measurements of HCHO columns, Environ. Res. Lett., 9, 114004, doi:10.1088/1748-9326/9/11/114004, 2014. 9211

AMTD
8, 9209–9240, 2015

Table 1. Fitting window and parameters used in the retrieval of H_2CO differential slant column densities.

Fitting window	327.7–356.0 nm
Radiance reference spectrum	Computed online over the remote Pacific ocean between 30° N and 30° S
Baseline polynomial	3rd order
Scaling polynomial	3rd order
Instrument slit function	Pre flight measurements
Solar reference spectrum	Chance and Kurucz (2010)
H_2CO cross-sections	Chance and Orphal (2011), 300 K
O_3 cross-sections	Malicet et al. (1995), 228 and 295 K
NO_2 cross-sections	Vandaele et al. (1998), 220 K
BrO cross-sections	Wilmouth et al. (1999), 228 K
O_2-O_2 collision complex cross-sections	Thalman and Volkamer (2013), 293 K
Molecular Ring cross sections	Chance and Spurr (1997)
Undersampling correction	Computed online, Chance et al. (2005)

AMTD
8, 9209–9240, 2015

Table 2. Systematic uncertainties of the cross sections included in the fitting of H_2CO.

Molecule	Data source	Cross section error %
H_2CO 300 K	Chance and Orphal (2011)	5 %
O_3 228 and 295 K	Malicet et al. (1995)	2 %
NO_2 220 K	Vandaele et al. (1998)	3 %
BrO 228 K	Wilmouth et al. (1999)	8 %
O_2–O_2 collision complex 293 K	Thalman and Volkamer (2013)	3 %
Molecular Ring	Chance and Spurr (1997)	5 %

AMTD
8, 9209–9240, 2015

Table 3. Geographical limits of the regions depicted in Fig. 5.

Region	Geographical limits
Pacific Ocean	30° S to 30° N 165 to 175° W
Southeastern US	30 to 41° N 77 to 95° W
Amazon Basin	15° S to 0° 50 to 70° W
Europe	40 to 52° N 0 to 25° E
Southeastern Asia	5° S to 5° N 95 to 120° E
Tropical Africa	1.5° S to 11° N 8° W to 30° E
Southern Africa	25 to 10° S 17 to 33° E
East China	28 to 39° N 111 to 120° E

AMTD
8, 9209–9240, 2015

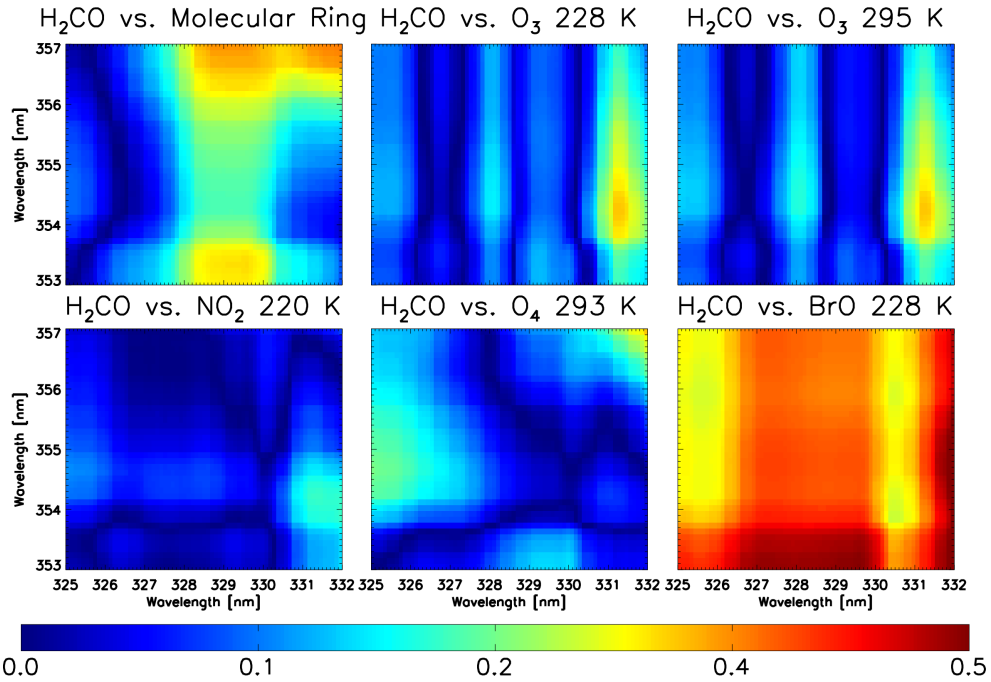

Figure 1. Correlation among H_2CO and different cross-sections for different fitting windows. The value of the *x* axis indicates the beginning of the fitting window and the *y* axis the end. The correlation values plotted here are the mean values for all the pixels in one orbit. Only pixels with solar zenith angles below 70° have been considered.

AMTD
8, 9209–9240, 2015

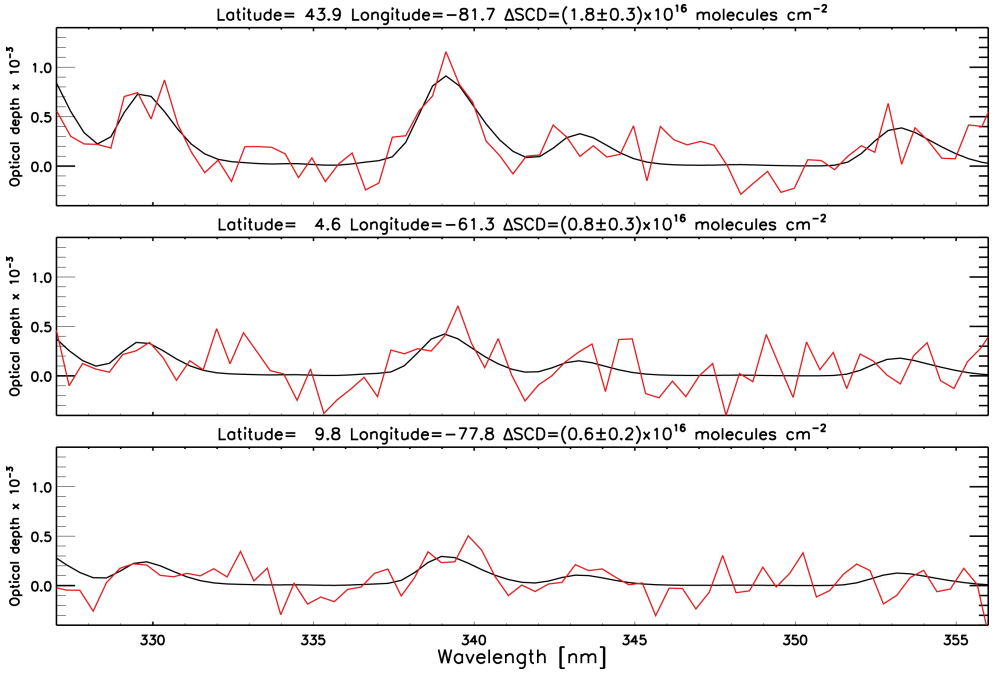

Figure 2. Fitting results of three pixels with decreasing concentrations of H_2CO in orbit 3538 outside the SAA. Black lines represent the fitted H_2CO optical depth, and red lines the fitted H_2CO optical depth plus the fitting residuals.

AMTD
8, 9209–9240, 2015

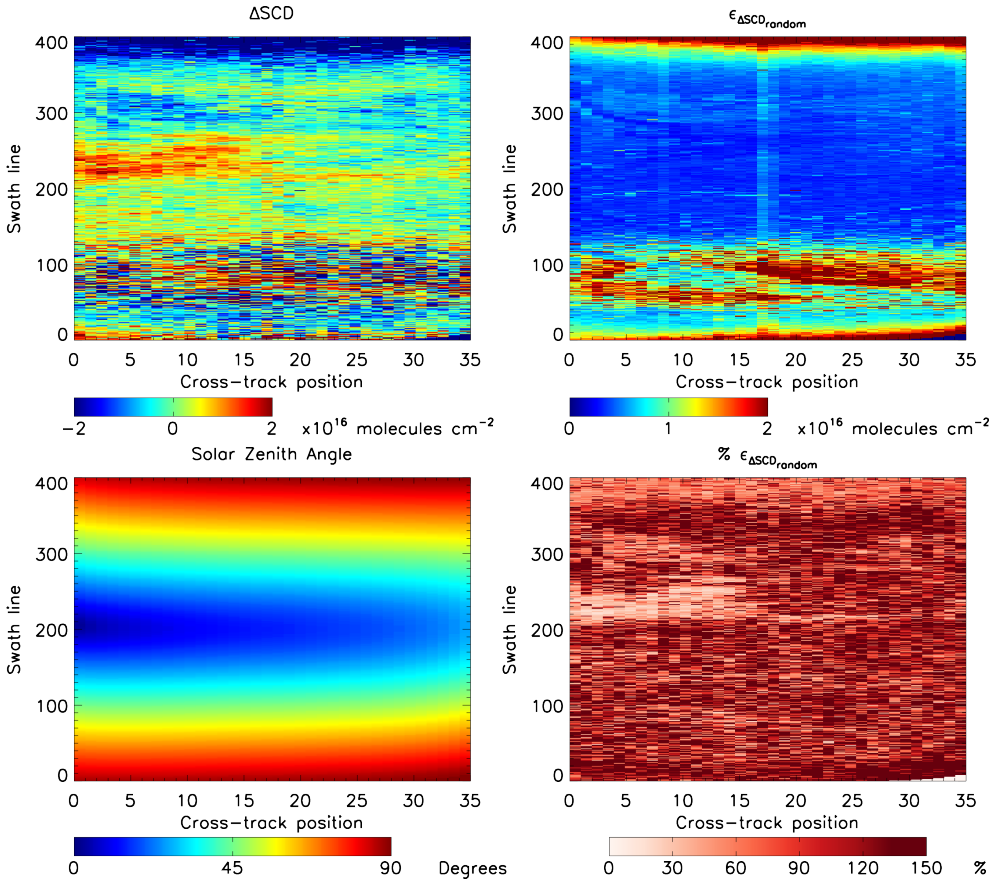

Figure 3. ΔSCD, fitting uncertainty, SZA and relative fitting uncertainty for orbit 3538. The effect of the SAA is clearly visible in the two top panels (swath lines 20 to 120). In the top right panel showing the fitting uncertainty it is possible to appreciate the effect of splitting the central cross-track pixel (Seftor et al., 2014).

AMTD
8, 9209–9240, 2015

SAO OMPS H_2CO retrieval

G. González Abad et al.

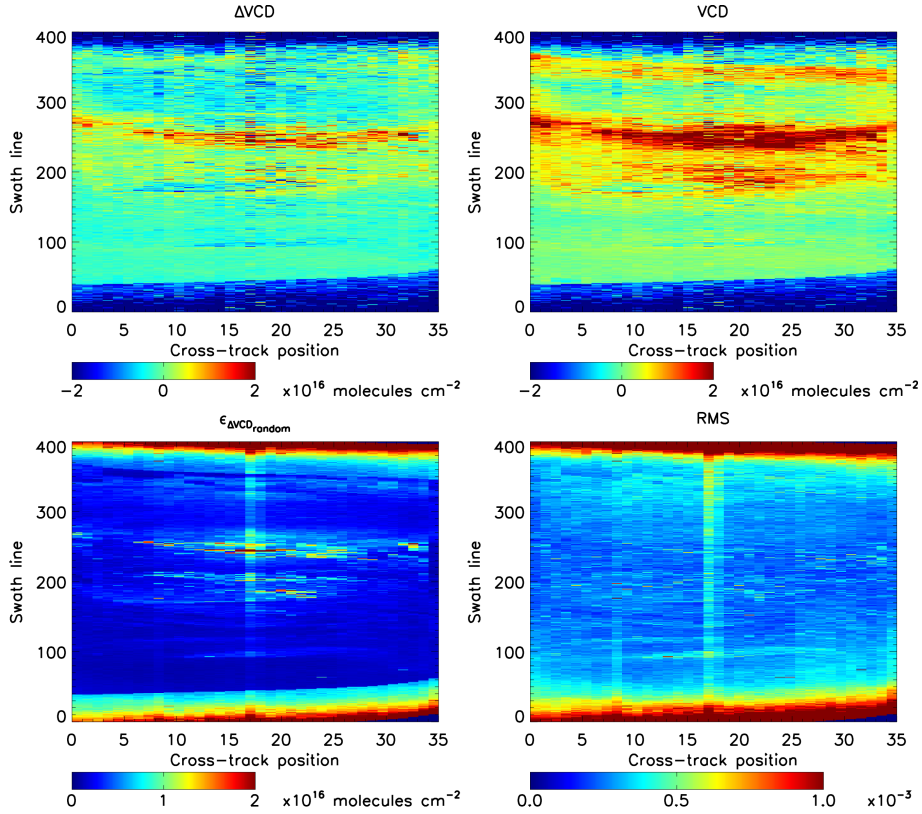

Figure 4. Retrieval for orbit 6202, January 2013 Africa and Europe overpass. VCDs corrected with the reference sector from the Ocean Pacific are depicted in top right panel while original ΔVCDs are shown in top left panel. Bottom two panels show the fitting uncertainty which shows no effect of the SAA in contrast with the ones shown in Figure 3 and RMS values where is possible to see the effect of splitting the central cross track pixel in two cross track positions (Seftor et al., 2014).

AMTD
8, 9209–9240, 2015

SAO OMPS H_2CO retrieval

G. González Abad et al.

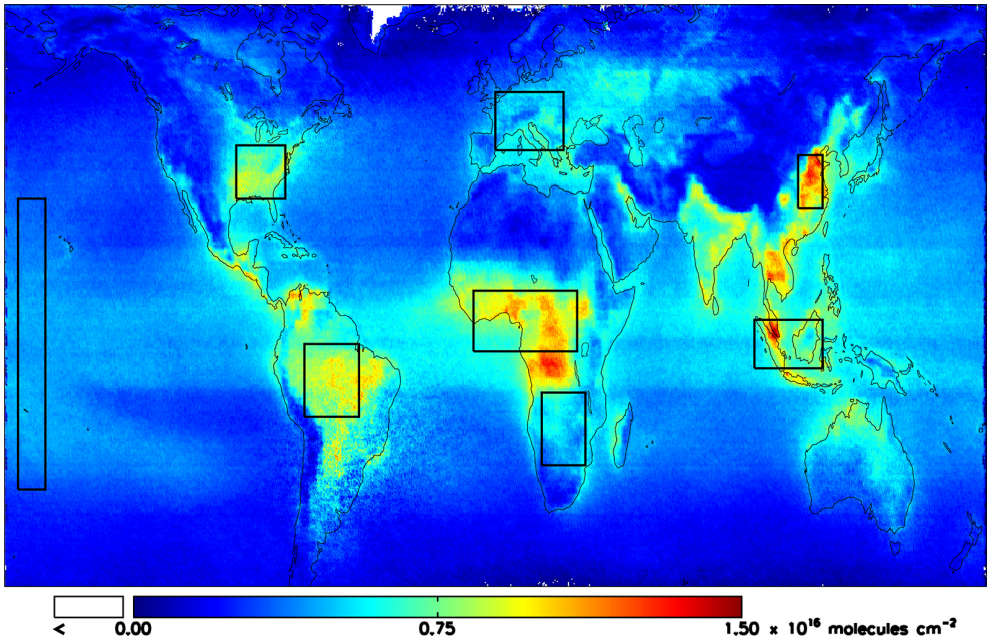

Figure 5. 2013 OMPS SAO H_2CO (January through September) global mean at a resolution of 0.25° × 0.25° showing the eight regions used in the comparison of OMPS SAO, OMI BIRA and OMI SAO retrievals. Seven of these regions have enhanced H_2CO concentrations linked to biogenic, anthropogenic and biomass burning processes. The eighth region, The Pacific Ocean, shows background concentrations of H_2CO due to CH_4 oxidation.

AMTD
8, 9209–9240, 2015

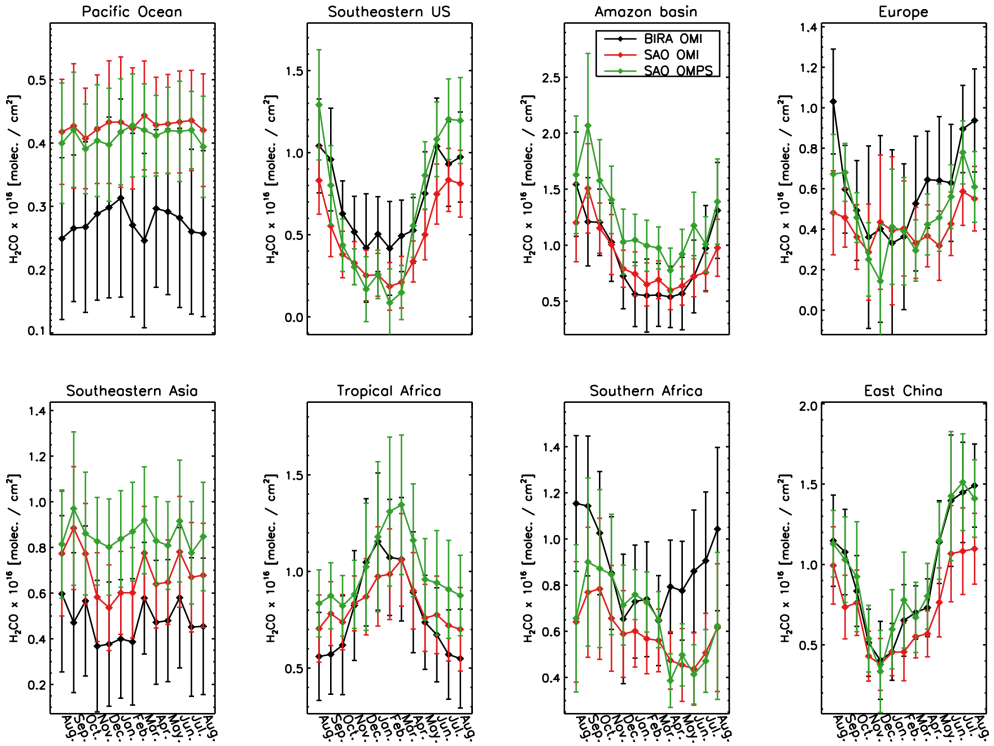

Figure 6. Monthly means between August 2012 and August 2013 for the eight regions depicted in Fig. 5. Error bars represent the standard deviation of the mean value with in the region. Green lines and data points represent OMPS SAO retrievals, red is used for OMI SAO and black for OMI BIRA. The shapes of seasonal cycles are reproduced similarly by the three retrievals despite having significant offsets which are further analyzed in Fig. 7.

AMTD
8, 9209–9240, 2015

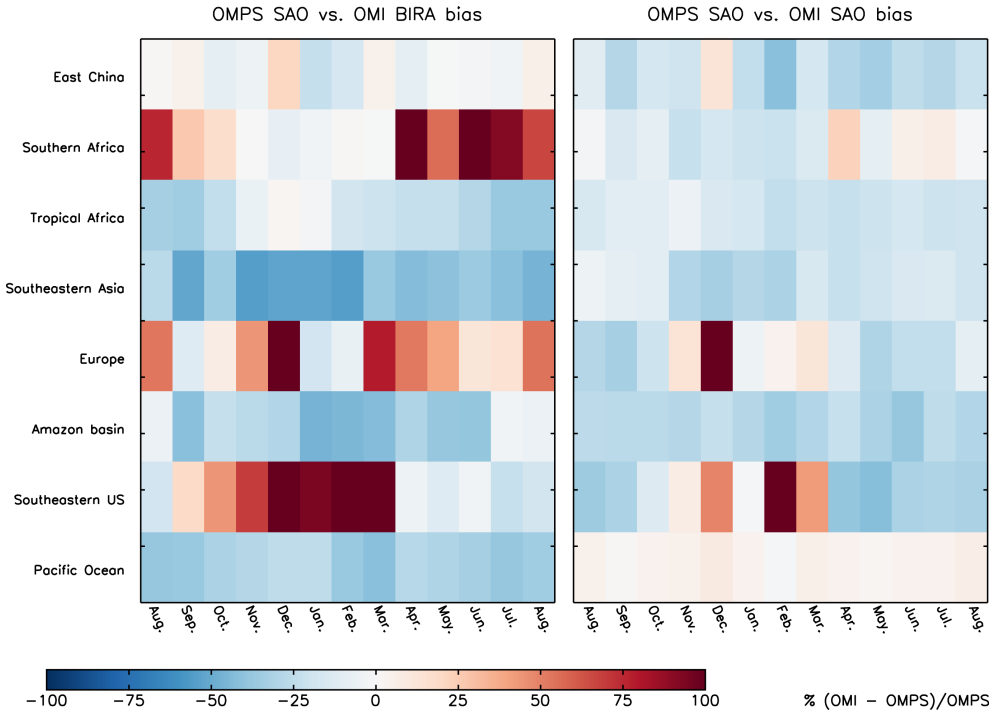

Figure 7. Monthly mean offsets between OMPS SAO retrieval and OMI retrievals from BIRA (left panel) and SAO (right panel). The offsets are expressed as percent of the OMI retrieval minus the OMPS retrieval. As expected the biases between OMPS SAO and OMI BIRA retrievals are bigger than the biases between OMPS SAO and OMI SAO. Southern Africa, Europe and Southeastern US show the most relevant differences.

AMTD
8, 9209–9240, 2015

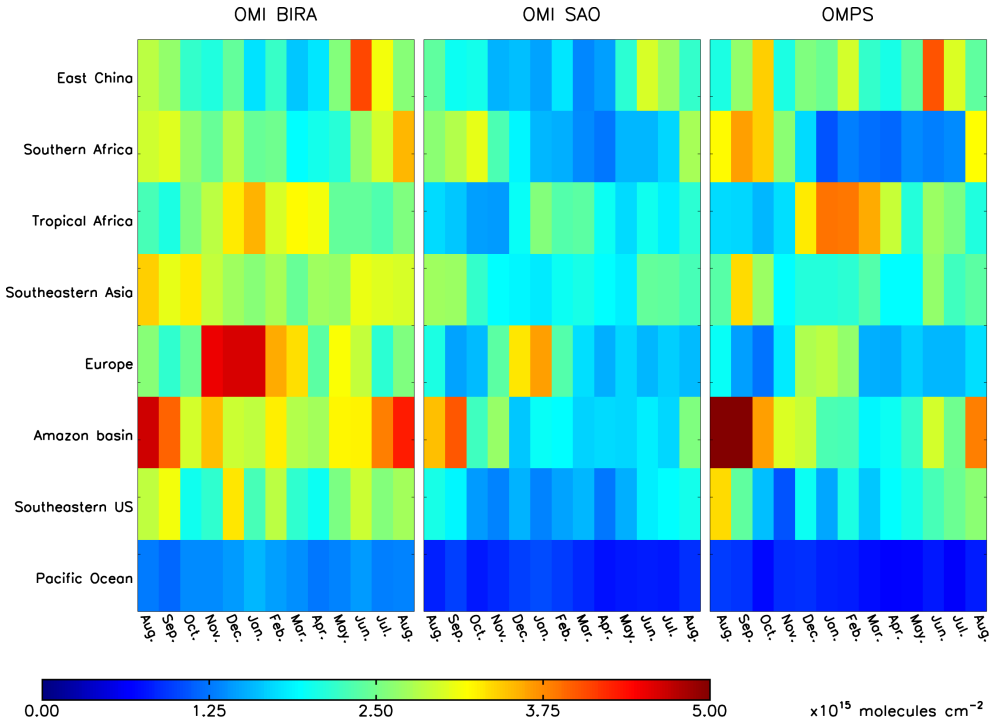

Figure 8. Standard deviation of the monthly means. Left panel OMI BIRA, middle panel OMI SAO and right panel OMPS SAO. Some regions show consistent enhanced standard deviations across retrievals for particular months, i.e. the Amazon basin between July and September and Tropical Africa between December and March. These high variabilities are linked to biomass burning episodes.

AMTD
8, 9209–9240, 2015